Direct Mapping of Spin Wave Modes of Individual $Ni_{80}Fe_{20}$ Nanorings

Chang Tian[1], Ushnish Chaudhuri[1,2], Navab Singh[3] and Adekunle O. Adeyeye[1,4]*

[1]Department of Electrical and Computer Engineering, National University of Singapore, 117576, Singapore.

[2]Physics Department, National University of Singapore, 117551, Singapore.

[3]Institute of Microelectronics, A*STAR, 2, Fusionopolis Way, 138634, Singapore.

[4]Present address: Department of Physics, Durham University.

*Corresponding author. E-mail: eleaao@nus.edu.sg

Abstract

Ferromagnetic nanorings exhibit tunable magnetic states with unique magnetization reversal processes and dynamic behavior that can be exploited in data storage and magnonic devices. Traditionally, probing the magnetization dynamics of individual ferromagnetic nanorings and mapping the resonance modes has proved challenging. In this study, micro-focused Brillouin light scattering spectroscopy is used to directly map the spin wave modes and their intensities in nanorings as a function of ring width and applied magnetic field. Micromagnetic simulations provide further insights into the experimental observations and are in good agreement with the experimental results. These results can help in improving the understanding of spin wave confinement in single elements for magnonic devices and waveguides.

Keywords Spin waves, Brillouin Light Scattering, Nanoring, OOMMF, Magnonics

1. Introduction

The static and dynamic behavior of micro or nano sized magnetic rings are of significant scientific interest since reports emerged highlighting its applications for data storage[1] and Biosensors [2]. Nanometer sized ferromagnetic metal rings with varying widths and thicknesses exhibit a variety of magnetic states, switching behavior and spin dynamics, which can be modified by changing the geometry, material composition or applied field [3,4,5]. Properly tuned, these rings at remanence are able to show a range of stable magnetic states such as the onion state (OS) or the flux closed vortex state (VS) [6]. This flux-closure VS is especially interesting since the magnetization (M) follows the ring edges either in a clockwise or counter-clockwise direction. Previously, the static behavior of magnetic rings including circular [7,8,9], elliptical [10,11] and rectangular rings [12,13] were extensively investigated. The switching properties of ferromagnetic ring elements have also been studied via magnetoresistance (MR) measurements [14,15,16]. MR is a very useful method to study the static behavior of nanorings since the MR signal does not diminish with decreasing elemental size, it possible to make resistive measurements on a single-element. However, for the dynamic properties, decreasing the ring size reduces the magnetic moments which significantly reduces the signal in conventional ferromagnetic resonance (FMR) measurements. Hence to study magnetization dynamics of nanorings using Vector network analyzer (VNA)-Coplanar waveguide (CPW) methods [17,18] or Brillouin light scattering (BLS) methods [19], array of nanorings are mainly used. These measurement approaches are however not very suitable for the detection of dynamics of Individual rings or for direct mapping of spin-wave intensity distributions. These limitations can be overcome by using a micro-focused BLS technique. Time resolved Magneto-Optical Kerr Effect (MOKE) spectroscopy is also another commonly used optical technique to detect magnetization dynamics in nanostructures [20,21].

These techniques help in understanding the dynamics of magnetic nanorings which is needed for the development of logic [22] and microwave devices [23].

In conventional BLS technique, the laser is focused on an area of several tens of micrometers. However, in this micro-focused BLS technique the laser spot is almost about 250 nm and the scattered light is collected from this highly focused area and analyzed. This technique thus has a high spatial resolution and one can also obtain a two-dimensional spin-wave intensity map consequently achieving a direct visualization of spin wave distribution.

In this study, the magnetization dynamics of individual ferromagnetic nanorings is systematically probed using micro-focused BLS spectroscopy as a function of applied field amplitude and ring size. Two-dimensional intensity maps of spin-waves were directly observed by raster-scanning the laser on the sample. Thereby, aiding our fundamental understanding of the magnetization dynamics of individual elements without the magnetostatic interactions from (i) the shape of the array boundary and (ii) the lattice arrangement influencing the ring due to interaction fields (like dipolar interactions) in the neighborhood [24,25]. The resonance frequency and the spin wave modes were found to be very sensitive to subtle changes in applied field amplitude and variation in ring widths. Micro-magnetic simulations were performed to support and aid our understanding of the experimental results. These simulations were in good agreement with the experimental results.

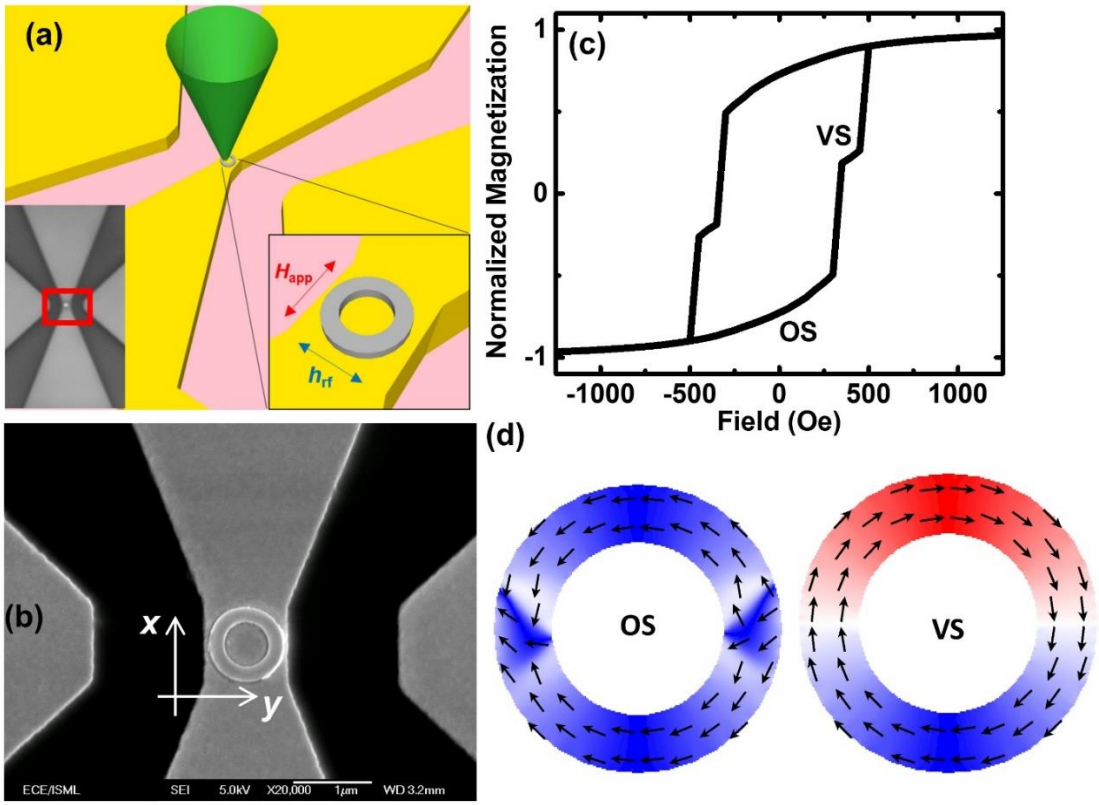

Figure 1. (a) Schematic of the experimental configuration for the micro-BLS measurement. The laser beam is focused onto the sample on the signal line of the CPW. Inset: CCD camera image of the sample. (b) SEM image of the ring on the signal line. (c) Simulated hysteresis loop for the 20-nm thick $Ni_{80}Fe_{20}$ ring (D = 1000 nm, d = 600 nm and w=200 nm). (d) Magnetization of the ring in the Onion state (OS) and vortex state (VS).

2. Experimental Methods and Simulation details

A single 20nm thick $Ni_{80}Fe_{20}$ nanoring was patterned on the signal line of ground-signal-ground (GSG)-type CPW with the ground and signal lines shorted at one end. The direction of the applied field (H_{app}) was defined as the 'x' direction and when placing the sample, the signal line of the CPW was oriented along this direction. This H_{app} was thus perpendicular to the generated RF magnetic field (h_{rf}), as shown in figure 1(a). An image of the nanoring on top of the CPW

from the charge-couple device (CCD) camera is shown in the inset of figure 1(a). The bright dot indicates the position of the laser spot. A zoomed-in scanning electron micrograph (SEM) of the ring used to measure the dimensions of the ring is shown in figure 1(b). The outer diameter, *D* is 1000 nm while the inner diameter, *d* is 600 nm. The width of the ring *w = (D-d)/2* is 200 nm. A schematic of the micro-focused BLS experiment is also shown in figure 1(a). The green cone is representative of the mono-chromatic BLS laser being focused down to the ring.

Individual nanorings were patterned on the signal line of GSG-type CPW using deep ultraviolet lithography (DUV). Further details regarding the fabrication process are in Ref:26. E-beam evaporation was used to deposit Cr (5 nm) / $Ni_{80}Fe_{20}$ (20 nm) at a rate of 0.2 Å/s, in a chamber with base pressure below 6 x 10^{-8} Torr, followed by a lift-off process. The Cr layer was used as an adhesive. The CPW was shorted by fabricating an adapter using optical lithography, followed by a deposition of Cr (5 nm)/Au (200 nm) and a subsequent lift-off process. Microwaves were generated by a single port signal high frequency source (Anritsu) in the shorted CPW using a pico-probe. The micro-focused BLS experiment uses a mono-chromatic laser focused down to ~250 nm on the ring. The scattered laser beam was analysed using a six pass tandem Fabry-Perot (TFP) interferometer. Further details of the micro-focused BLS setup can be found in Ref:27. Before measuring the BLS spectra, the individual rings were pre-saturated at 2200 Oe. H_{app} was slowly decreased from +1200 Oe to -1200 Oe. The spin waves were generated in the ring due to the interaction of the h_{rf} with the magnetization of the ring.

Micromagnetic simulations using the OOMMF software were performed for the sample at T = 0 K. We list the simulation parameters used for the $Ni_{80}Fe_{20}$ (Permalloy, Py) nanoring: The saturation magnetization M_S was taken as 800 emu/cm^3 while the exchange constant *A* was equated to 13×10^{-7} erg/cm. The magneto-crystalline anisotropy (K_1) can be assumed to be negligible (0

erg/cm^3) in the simulations since the shape anisotropy of a patterned nanostructure is greater than the magneto-crystalline anisotropy of bulk Py. The dimensions obtained using the SEM image were used to make the mask of the pattern. A unit cell of 5 × 5 × 5 nm^3 was used to simulate the static magnetization. To simulate the static magnetization reversal, the damping coefficient, α was taken as 0.5 for rapid convergence. Time-dependent, dynamic magnetization, simulations were performed using excitation field: $h_{sinc} = h_0 \frac{((sin(2\pi ft)))}{t}$ along the 'y' direction, where h_0 = 50 Oe. Gyromagnetic ratio ($\gamma/2\pi$) was taken as 2.8 GHz/kOe and the damping coefficient, α was 0.008. The cutoff frequency for the dynamic simulations was 14 GHz. To produce a uniform excitation in the frequency domain, a sinc wave was used in these simulation. Simulation results of the magnetization dynamics were obtained in the time domain which were converted into the frequency domain using Fast Fourier Transform (FFT). The frequencies with which M_y oscillates corresponds to the spin wave modes. The time scale data along with other simulation details can be found in the supplementary materials.

3. Results and Discussions

To understand the field evolution of the magnetization reversal process of the nanoring before the BLS measurements, we simulated the hysteresis loop of the nanoring using the OOMMF code from NIST [28]. The ring dimensions obtained from the SEM image were used for the simulation. As shown in figure 1(c) the micromagnetic simulation revealed a two-step switching. At a large negative saturation field, the magnetic moments of the ring were aligned along the field direction. As the applied magnetic field was decreased towards 0 Oe, the magnetic moments start to relax along the circumference of the ring to form the OS. The first switching occurs at 300 Oe, corresponding to the transition from the OS to VS. During this transition, one of the 180° domain

walls travels along one arm of the ring and annihilates the other 180° domain to form the VS. The second switching step at around 450 Oe corresponds to the transition from the VS to a reverse OS. The reverse OS is formed due to the nucleation of a magnetic domain in the part of the ring with the magnetization opposite to the direction of H_{app}, which propagates to the other end of the ring. As H_{app} is further increased, the magnetic moments are saturated once again along the field direction. The simulated magnetization states for both the OS and VS are shown in figure 1(d).

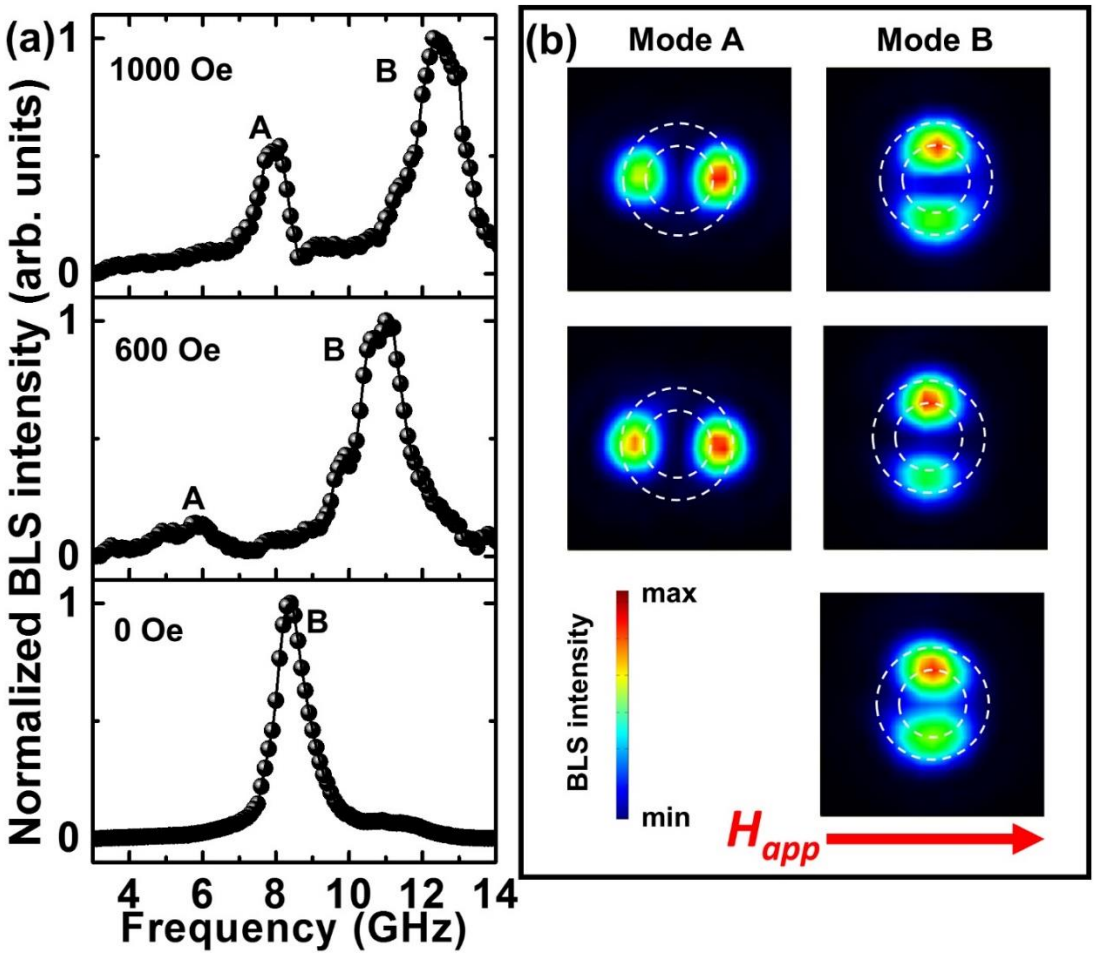

Figure 2. (a) BLS spectra as a function of the applied field for the ring with w=200 nm. (b) Two-dimensional BLS intensity maps overlaid with the contours of the ring for the observed modes.

In figure 2(a), the BLS spectra from a $Ni_{80}Fe_{20}$ nanoring of w = 200nm is presented for varying magnetic fields. For H_{app} = 1000 Oe, we observed two prominent peaks at 8.0 GHz and

12.3 GHz corresponding to position of mode A and mode B respectively. In order to identify the mode profile, we performed 2-dimentional (2-D) raster-scanning on the ring along the *x* and *y* axis over an area of 2 μm × 2 μm. The measured 2-D maps of BLS intensity overlaid with the contours of the ring are shown in figure 2(b). Since the BLS response is proportional to the intensity of the dynamic magnetization, mode A corresponds to a large intensity of spin waves at the equatorial regions of the ring, while for mode B the intensity is concentrated at the pole regions of the ring. When H_{app} is decreased to 600 Oe, a weak mode at 5.8 GHz and a strong mode at 11 GHz is observed as shown in figure 2(a). Using the 2-D maps for the modes, we have identified the two modes by their spatial characteristics as shown in figure 2(b). The mode at 5.8 GHz corresponds to mode A, i.e. spin waves are concentrated at the equatorial regions while the mode at 11 GHz corresponds to mode B, with the intensity largest at the poles. The resonance frequencies of both mode A and B decrease as the amplitude of H_{app} is decreased. The decrease in BLS intensity for mode A may be attributed to the fact that the magnetization at the equatorial regions of the ring tends to relax along the circumference of the ring and be parallel with h_{rf} when H_{app} is decreased. When H_{app} is further reduced to 0 Oe, only one prominent peak at 8.4 GHz which corresponded to mode B is observed.

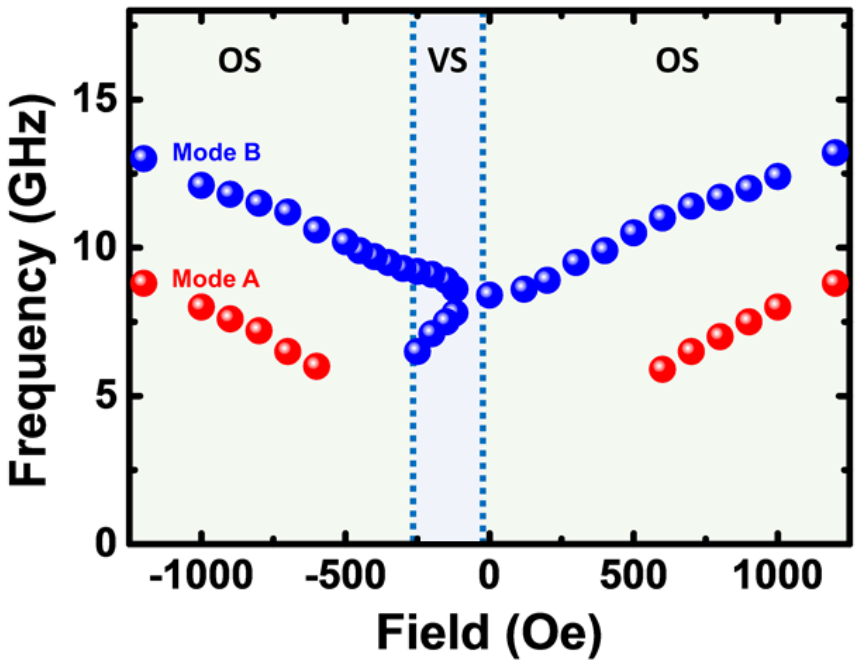

Figure 3. Experimental resonance frequency of the prominent peaks versus the applied field for the ring with *w*=200 nm. Vortex state (VS) is identified when H_{app} is between -120 Oe and -250 Oe and the Onion state (OS) exists for rest of the field range.

The field evolution of the dynamic behavior of the rings has been systematically investigated by sweeping H_{app} from +1200 Oe to -1200 Oe while acquiring the BLS spectra for every 100Oe. We have extracted the resonance frequencies for modes A and B from the BLS spectra and plotted it as a function of H_{app} in figure 3. One can clearly identify, two distinct regions associated to the OS and the VS. In the region marked OS, the resonance frequencies of mode A and B are linearly dependent with H_{app} when H_{app} > -120 Oe. Mode B undergoes a splitting when the VS is formed in the applied field range between -120 Oe and -250 Oe. The spin wave mode splits due to the opposite direction of magnetization at the top and bottom poles when the VS is formed. In this magnetic state, the poles with magnetization antiparallel to the H_{app} direction exhibits a negative dispersion in resonance frequency ($df_r/dH_{app} < 0$) while the other arm with magnetization parallel to H_{app} exhibits a positive dispersion ($df_r/dH_{app} > 0$) [17]. It has been

previously reported that, the lower frequency mode in this region shows a tendency to soften when approaching the transition to the saturated state [29]. This mode can thus aid in magnetization reversal in an arm of a nano ring and has found application in microwave-assisted switching of micrometric rings [30].

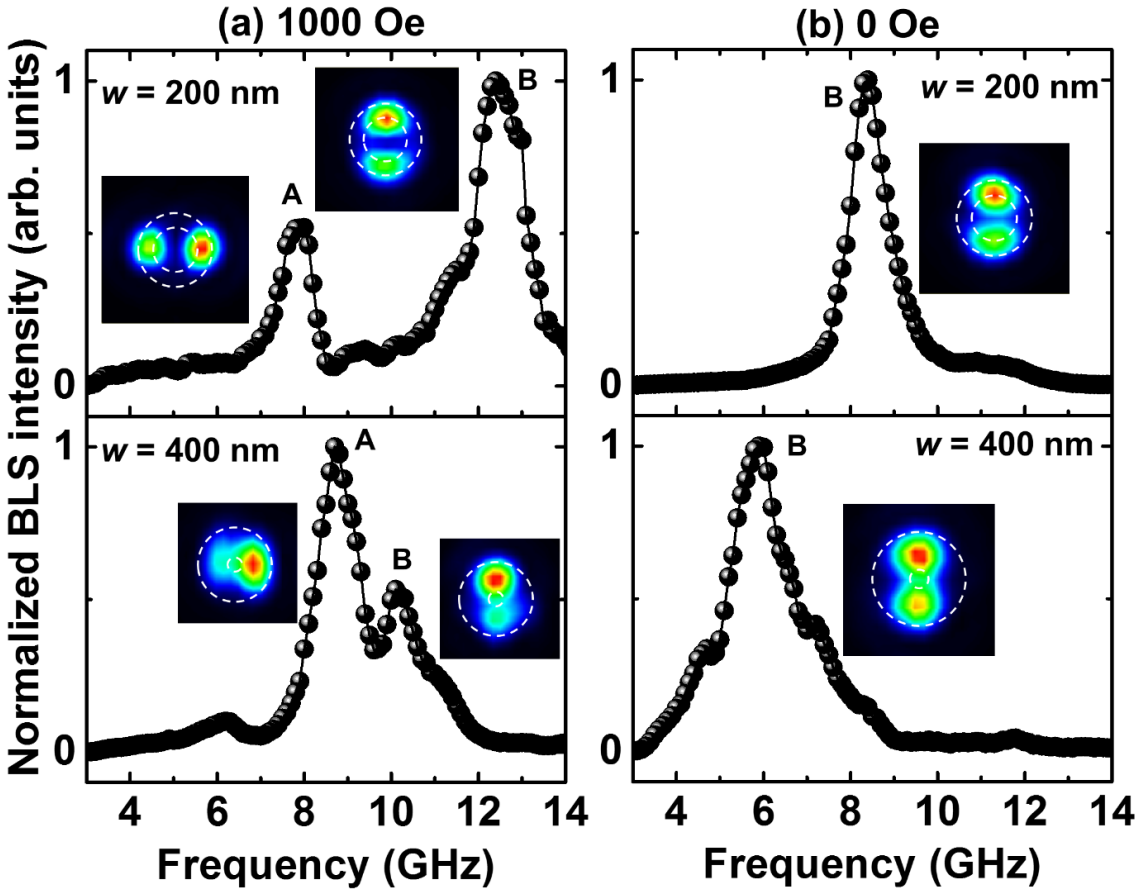

Figure 4. BLS spectra for rings with w=200 nm and 400 nm when H_{app} equals (a) 1000 Oe and (b) 0 Oe. Inserts are the corresponding to the 2-D BLS intensity maps for mode A and B.

The effect of ring width on the dynamic behavior was also investigated by comparing BLS responses of two rings of identical outer diameter D =1000 nm with varied inner ring diameters of

600 nm and 200 nm which corresponds to the rings with width of 200 nm and 400nm respectively. In figure 4(a), the resonance frequencies of modes A and B seem to converge for the ring with *w* = 400 nm in contrast to the ring with *w* = 200 nm which showed a frequency gap of 4.3 GHz between the two modes. The resonance frequency of mode A increased from 8.0 GHz to 8.7 GHz when ring width was increased, while the resonance frequency of mode B decreased from 12.3 GHz to 10.1 GHz. The resonance frequencies of modes A and B are determined by the ring width due to the effect of demagnetizing fields. For both the rings, the resonance in the equatorial direction of the rings correspond to mode A. Mode B corresponds to the orientation when H_{app} was oriented parallel to the easy axis while mode A corresponds to the H_{app} oriented along the hard axis. Shown as inserts are the 2-D maps for the two modes. The Kittel formula can be used to explain the behavior of modes A and B occurring at the equatorial or polar sections of the ring[31]:

$$f_r = \frac{\gamma}{2\pi}\sqrt{\left(H_{eff} + (N_z - N_x)M_x\right)\left(H_{eff} + \left(N_y - N_x\right)M_x\right)} \qquad (1)$$

where f_r is the resonance frequency, N_x, N_y and N_z are the demagnetizing factors for *x*, *y* and *z* directions. $N_x + N_y + N_z = 4\pi$, $\gamma/2\pi$ is the reduced gyromagnetic ratio, $4\pi M_x$ is the magnetization of the sample along the x-direction and H_{eff} is the effective field along this direction. On completely saturating the ring along a particular direction, M_x will be equal to M_s, the saturation magnetization. In the case of mode A, the H_{eff} is reduced by the internal demagnetization ($H_{eff} = H_{app} - |H_{demag}|$) and hence a reduction of resonance frequency is observed. H_{demag} refers to the demagnetization fields inside the ring structure. The demagnetization fields for both the samples with w=200 nm and 400 nm are presented in the supplementary material. Mode A experiences a larger demagnetizing field than mode B since the moments in mode A are forced to be perpendicular to the ring circumference. The demagnetizing field is opposite to the magnetization and it increases

as the width of ring decreases. Therefore, mode A experiences a lower internal field and hence lower resonance frequency of mode A when compared with mode B. As the ring width is increased, the internal field and resonance frequency for mode A are expected to increase. This causes mode A to shift to a higher frequency for the sample with w = 400nm.

The BLS spectra at 0 Oe for w = 200 and 400 nm are shown in figure 4(b). As expected, the resonance frequency of mode B decreases with increase of the width of the ring. The resonance frequencies are 8.4 and 5.9 GHz for w = 200 and 400 nm, respectively. The shape anisotropy field increases as the width of the ring decreases, thus the narrow ring, w = 200nm has a higher resonance frequency for mode B. The corresponding 2-D maps for the two modes are also shown as inserts in figure 4(b). In the supplementary material, the BLS spectra from a ring with D=1000 nm and w=150 nm is presented, to illustrate the effect of a reduction in ring width.

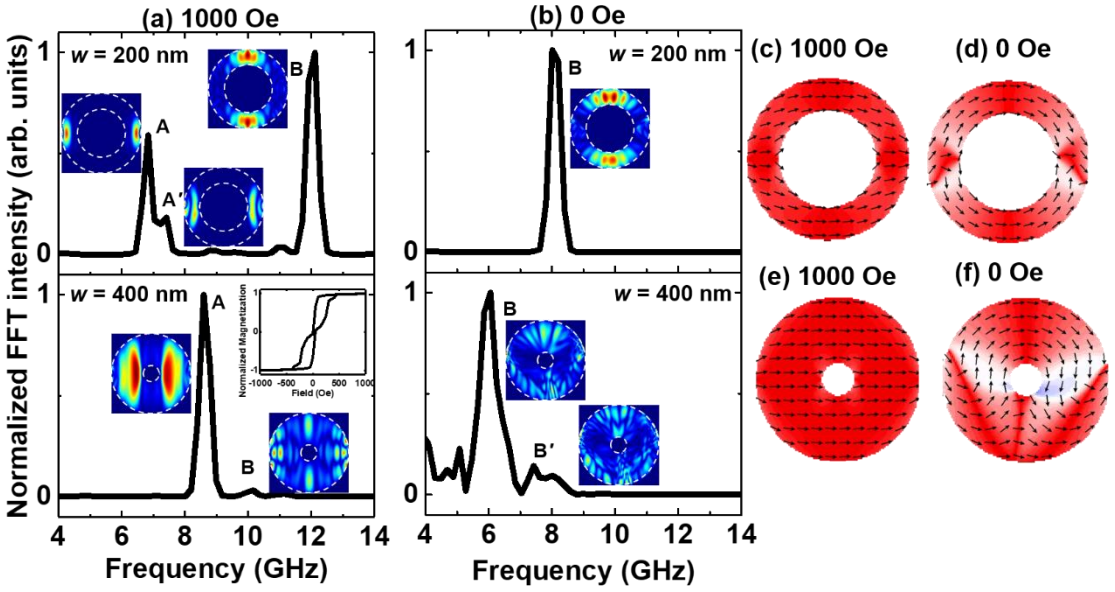

Figure 5. Simulated dynamic spectra for rings with w=200 nm and 400 nm when H_{app} equals (a) 1000 Oe and (b) 0 Oe. Inserts are the corresponding simulated 2-D spatial mode profiles for mode A and B. Inset in (a) for w = 400nm illustrates the simulated hysteresis loop. (c) and (d) are the static magnetization states

for the ring with w=200 nm at 1000 Oe and 0 Oe while (e) and (f) are the static magnetization states for the ring with w=400 nm.

Dynamic micromagnetic simulations were performed using OOMMF as shown in figure 5 depicting the simulated dynamic spectra for nanorings with w = 200 nm and w = 400 nm as a function of H_{app}. These simulations were in good agreement with the experimental results shown in figure 4. For H_{app} = 1000 Oe, the resonance frequencies of mode A are 6.8 and 8.6 GHz and mode B are 12.1 and 10.2 GHz for w = 200 and 400 nm respectively. Mode A is localized at the equatorial regions while mode B is localized along the poles which is in agreement with our experimental observation. Mode A is more intense than mode B for the ring of w = 400 nm because the area of resonance is larger than that of mode B. The corresponding simulated mode profiles are shown as inserts next to the peak positions. For w=200 nm, there appears to be a satellite mode at 7.4 GHz which can be identified as a higher-order mode with non-zero wave number due to the confined geometry. Satellite peaks may not be visible in the experimental BLS response due to the line width of the main mode being too broad which makes the satellite peaks indistinguishable. the At H_{app} = 0 Oe, the resonance frequency of mode B decreases from 8.0 GHz to 6.0 GHz when the width of the ring is increased from 200 nm to 400 nm. The mode profile is similar to that of mode B at 1000 Oe and it can be seen that the spin-wave intensity extends along the circumference of the ring. These results are in good agreement with the experimental observations. A mismatch between the experimental and simulated results may originate from imperfections in the fabricated nanoring or a minor misalignment of H_{app}. A small discrepancy in these factors can affect the static simulations which in turn can affect the dynamical simulation results.

Conclusions

To conclude, the magnetization dynamics in individual ferromagnetic nanorings are systematically probed using micro-focused BLS spectroscopy as a function of applied field amplitude and ring size. Magnetization dynamics in the various quasi-saturated regions of a nanoring were investigated and two-dimensional spin-wave intensity was directly mapped by raster-scanning the laser spot on the sample. Localization of spin waves was observed in the polar and equatorial regions. The localized spin waves were qualitatively explained using micromagnetic simulations, which were in good agreement with the experimental results. Our demonstration of tuning the spin wave modes by varying the ring widths may find applications in high speed storage and microwave devices.

Supplementary Materials

In the supplementary material section A, we discuss the static and dynamic simulations in greater details. In section B, a regular ring of D=1000 nm and w= 150 nm was measured and analyzed using micromagentic simulations. The effects of a defect were also discussed in this section. In section C, the BLS spectra is presented corresponding to the location on the ring where the laser was focused. In section D, the BLS spectrum is presented for the ring of w = 200 nm in the vortex state and in section E, the simulated demagnetization fields of a ring of w=200nm and w=400nm is illustrated.

Acknowledgements

This work was supported by the Ministry of Education, Singapore Tier 2 funding via grant number: R-263-000-C61-112. A.O.A. is a member of the Singapore Spintronics Consortium (SG-SPIN).

References

[1] J.-G. Zhu, Y. Zheng and G. A. Prinz, J. Appl. Phys. **87**, 6668 (2000).

[2] M. M. Miller, G. A. Prinz, S.-F. Cheng and S. Bounnak, Appl. Phys. Lett. **81**, 2211 (2002).

[3] H. Schultheiss, S. Schäfer, P. Candeloro, B. Leven, B. Hillebrands and A. N. Slavin, Phys. Rev. Lett. **100**, 047204 (2008).

[4] Y. Luo, Y. Du and V. Misra, Nanotechnology **19**, 265301 (2008**).**

[5] C. A. Ross, F. J. Castaño, W. Jung, B. G. Ng, I. A. Colin and D. Morecroft, J. Phys. D **41**, 113002 (2008).

[6] C. A. F. Vaz, T. J. Hayward, J. Llandro, F. Schackert, D. Morecroft, J. A. C. Bland, M. Kläui, M. Laufenberg, D. Backes, U. Rüdiger, F. J. Castaño, C. A. Ross, L. J. Heyderman, F. Nolting, A. Locatelli, G. Faini, S. Cherifi and W. Wernsdorfer, J. Phys. Condens. Matter **19**, 255207 (2007).

[7] C. A. F. Vaz, M. Kläui, J. A. C. Bland, L. J. Heyderman and F. Nolting, J. Appl. Phys. **95**, 6732 (2004**).**

[8] L. J. Heyderman, M. Kläui, B. Nöhammer, C. A. F. Vaz, J. A. C. Bland and C. David, Microelectron. Eng. **73**, 780 (2004).

[9] C. A. F. Vaz, M. Kläui, J. A. C. Bland, L. J. Heyderman, C. David and F. Nolting, Nucl. Instrum. Methods Phys. Res. B **246**, 13 (2006).

[10] S. H. Liou, R. F. Sabiryanov, S. S. Jaswal, J. C. Wu and Y. D. Yao, J. Magn. Magn. Mater. **1270**, 226 (2001).

[11] C. Yu, T. W. Chiang, Y. S. Chen, K. W. Cheng, D. C. Chen, S. F. Lee, Y. Liou, J. H. Hsu and Y. D. Yao, Appl. Phys. Lett. **94**, 233103 (2009).

[12] G. Shimon, A. O. Adeyeye and C. A. Ross J. Appl. Phys. **111**, 013909 (2012).

[13] G. Shimon, A. O. Adeyeye and C. A. Ross, Phys. Rev. B **89**, 024302 (2014).

[14] M. Kläui, C. A. F. Vaz, J. Rothman, J. A. C. Bland, W. Wernsdorfer, G. Faini and E. Cambril, Phys. Rev. Lett. **90**, 097202 (2003).

[15] F. J. Castaño, D. Morecroft and C. A. Ross, Phys. Rev. B **74**, 224401 (2006).

[16] M. Kläui, C. A. F. Vaz, W. Wernsdorfer, E. Bauer, S. Cherifi, S. Heun, A. Locatelli, G. Faini, E. Cambril, L. J. Heyderman and J. A. C. Bland, Physica B **343** (2004).

[17] F. Giesen, J. Podbielski, B. Botters and D. Grundler, Phys. Rev. B, **75**, 184428 (2007).

[18] J. Ding, M. Kostylev and A. O. Adeyeye, Appl. Phys. Lett. **100**, 062401 (2012).

[19] G. Gubbiotti, M. Madami, S. Tacchi, G. Carlotti, H. Tanigawa, T. Ono, L. Giovannini, F. Montoncello and F. Nizzoli, Phys. Rev. Lett. **97**, 247203 (2006).

[20] A. Barman , T. Kimura, Y. Otani, Y. Fukuma, K. Akahane, and S. Meguro, Rev. Sci. Instrum. **79**, 123905, (2008).

[21] C. Banerjee, S. Saha, S. Barman, O. Rousseau, Y. Otani, and A. Barman, J. Appl. Phys. **116**, 163912, (2014).

[22] H. Jung, Y.S. Choi, K.S. Lee, D.S. Han, Y.S. Yu, M.Y. Im, P. Fischer, and S.K. Kim, ACS nano **6**, 3712, (2012).

[23] G. Tong, Y. Liu, T. Cui, Y. Li, Y. Zhao, and J. Guan, Appl. Phys. Lett **108**, 072905 (2016).

[24] S. Saha, R. Mandal, S. Barman, D. Kumar, B. Rana, Y. Fukuma, S. Sugimoto, Y. Otani, Y. and A. Barman, Adv. Funct. Mater. **23**, 2378 (2013).

[25] V. V. Kruglyak, P. S. Keatley, R. J. Hicken, J. R. Childress, and J. A. Katine, Phys. Rev. B. **75**, 024407, (2007).

[26] A. O. Adeyeye and N. Singh, J. Phys. D **41**, 153001 (2008).

[27] A. Haldar, C. Tian and A. O. Adeyeye, Sci. Adv. **3**, e1700638 (2017).

[28] M. J. Donahue and D. G. Porter, Interagency Report NISTIR 6376, National Institute of Standards and Technology, Gaithersburg, MD,1999.

[29] F. Montoncello, L. Giovannini, and F. Nizzoli, J. Appl. Phys. **103**, 083910 (2008).

[30] J. Podbielski, D. Heitmann, and D. Grundler, Phys. Rev. Lett. **99**, 207202 (2007).

[31] C. Kittel, Phys. Rev. **73**, 155 (1948).